DISTRIBUTION FUNCTIONS FOR CUSPY DARK MATTER DENSITY PROFILES

LAWRENCE M. WIDROW
Department of Physics, Queen's University, Kingston, Ontario, Canada K7L 3N6; widrow@astro.queensu.ca

ABSTRACT

Various analytic expressions have been proposed for the density profile of dark matter halos. We consider six of these expressions for which the density profile has a power-law falloff $\rho \propto r^{-3}$ at large radii and a power-law cusp $\rho \propto r^{-\gamma}$ ($\gamma = 0, \frac{1}{2}, 1, \frac{3}{2}$) at small radii. The phase-space distribution function for these models is calculated assuming spherical symmetry and either an isotropic velocity dispersion tensor or an anisotropic dispersion tensor of the type proposed by Osipkov and Merritt. The differential energy distribution for these models is also derived. Several applications are discussed, including the analysis of dark matter search experiments and the study of halo formation in a cosmological setting. Analytic fitting formulae for some of the models are provided.

Subject headings: galaxies: halos — galaxies: kinematics and dynamics — dark matter

1. INTRODUCTION

A fundamental problem in modern astrophysics is to determine the nature of relaxed systems such as galaxies and dark matter halos. *N*-body methods are used extensively in this effort and allow one to follow explicitly the evolution of the phase-space distribution function (DF) *f*. A complementary approach seeks to obtain analytic steady state models. Essential to this task is the Jeans theorem which states that the DF for any equilibrium system can be written in terms of the integrals of motion. In addition it is often possible to make an educated guess as to the form of the DF. Lynden-Bell (1967), Tremaine (1987), and Merritt, Tremaine, & Johnstone (1989), for example, analyze model DFs that are designed to capture the physics of violent relaxation. By contrast, Henriksen & Widrow (1999) propose a DF that is motivated by the spherical infall model wherein particle energies vary in a more orderly fashion.

Unfortunately, neither the DFs considered by Merritt et al. (1989) nor the DF considered by Henriksen & Widrow (1999) lead to density profiles in agreement with those found in the simulations. The alternative is to begin with a desired expression for the density profile, together with simplifying assumptions about the shape of the velocity ellipsoid, and construct the DF using standard techniques (e.g., Binney & Tremaine 1987, hereafter BT). Occasionally, one is lucky and finds an analytic DF-density profile pair, as with the Hernquist model (Hernquist 1990). Although for more general profiles such as the so-called "γ-models" (see Carollo, de Zeeuw, & van der Marel 1995 and references therein) numerical integration is required, the problem is entirely tractable.

The γ-models, which include the Hernquist model as a special case, have a density profile with a power-law cusp $\rho \propto r^{-\gamma}$ at small radii and a $\rho \propto r^{-4}$ falloff at large radii. While these models have proved to be useful in the study of elliptical galaxies, the dark matter halos found in cosmological simulations appear to have a power-law falloff at large radii that is more gradual than r^{-4}. Navarro, Frenk, & White (1996) suggest that the density profiles of dark halos have a "universal" shape (the so-called NFW profile) of the form

$$\rho_{\text{NFW}} = \frac{\rho_0}{(r/a)(1 + r/a)^2} . \qquad (1)$$

They obtain reasonably good fits using this expression for halos that range in mass from $3 \times 10^{11} M_\odot$ (dwarf galaxies) to $3 \times 10^{15} M_\odot$ (rich galaxy clusters). However, there is considerable debate over just what the profile is in the innermost regions of a halo. Kravtsov et al. (1998) find that the observed rotation curves of dwarf and low surface brightness galaxies can be fitted by a profile with a shallower central cusp ($\rho \propto r^{-\gamma}$, where $\gamma \simeq 0.2$), and their own *N*-body simulations support this conclusion. On the other hand, Moore et al. (1998) have performed high-resolution simulations of cluster-sized halos and find a central cusp that is steeper than r^{-1} ($\gamma \simeq 1.4$).

Kravtsov et al. (1998) advocate a general fitting formula of the form

$$\rho = \frac{C\rho_0}{(r/a)^\gamma [1 + (r/a)^\alpha]^{(\beta-\gamma)/\alpha}} ; \qquad (2)$$

γ controls the slope of the inner profile, β that of the outer profile, and α the sharpness of the transition. The normalization parameter C will be discussed below. The NFW profile corresponds to $(\alpha, \beta, \gamma) = (1, 3, 1)$, while the γ-models correspond to $(\alpha, \beta, \gamma) = (1, 4, \gamma)$, with the Hernquist profile appearing as the special case $\gamma = 1$.

In this work, we derive semianalytic DFs for a select subset of the models described by equation (2). Specifically, we focus on models with an r^{-3} density falloff at large radii ($\beta = 3$). Furthermore, we consider only the six models for which the gravitational potential can be expressed in terms of elementary functions, namely, $\alpha = 1$; $\gamma = 0, \frac{1}{2}, 1, \frac{3}{2}$ and $\alpha = 2$; $\gamma = 0, 1$.

In § 2 the DFs for the six models assuming an isotropic velocity dispersion tensor are calculated. DFs with anisotropic velocity dispersion of the Osipkov-Merritt type are considered in § 3, and their existence and stability is discussed. In § 4 the differential energy distribution of various models is calculated. Several possible applications of our results are discussed in § 5. Analytic fitting formulae for many of the DFs found in the text are provided in the Appendix.

2. SYSTEMS WITH ISOTROPIC DISPERSION TENSORS

For convenience we introduce the dimensionless variables $R \equiv r/a$, $V \equiv v/(4\pi G\rho_0 a^2)^{1/2}$, $\varrho = \rho/\rho_0$, and $F = (4\pi G)^{3/2}a^3\rho_0^{1/2} f$. In addition, we define the relative energy and relative potential (again in dimensionless form) to be respectively $\mathscr{E} \equiv -(E - \Phi_\infty)/4\pi G\rho_0 a^2$ and $\Psi \equiv -(\Phi - \Phi_\infty)/4\pi G\rho_0 a^2$, where $E \equiv \frac{1}{2}v^2 + \Phi$ and $\Phi = \Phi(r)$ is the Newtonian potential with $\Phi(\infty) \equiv \Phi_\infty$.

In general, the Newtonian potential calculated from the density profile with $\beta = 3$ must be determined numerically. [For the γ-models ($\alpha = 1$; $\beta = 4$) an analytic form for the potential not only exists but can be inverted to give $r = r(\Phi)$ in closed form.)] However, the potential can be determined analytically for $\alpha = 1$; $\gamma = 0, \frac{1}{2}, 1, \frac{3}{2}$ (models I–IV), and $\alpha = 2$; $\gamma = 0, 1$ (models V, VI), and for convenience, we focus on these six cases. Expressions for the potentials are collected in Table 1. The normalization parameter C in equation (2) is chosen so that for $\Psi(0) = 1$ it has the limiting

TABLE 1

NEWTONIAN POTENTIALS FOR SELECTED DENSITY PROFILES

Model	α	γ	C	Ψ
I........	1	0	2	$\frac{2}{R}\ln(1+R) - (1+R)^{-1}$
II.......	1	$\frac{1}{2}$	$\frac{3}{2}$	$1 - \frac{3+R}{(R+R^2)^{1/2}} + \frac{3}{2R}\ln S$
III......	1	1	1	$\frac{1}{R}\ln(1+R)$
IV......	1	$\frac{3}{2}$	$\frac{1}{2}$	$1 - \left(\frac{1+R}{R}\right)^{1/2} + \frac{1}{2R}\ln S$
V.......	2	0	1	$\frac{1}{R}\sinh^{-1}(R)$
VI......	2	1	$\frac{2}{\pi}$	$1 - \frac{2}{\pi}\tan^{-1}(R) + \frac{1}{\pi R}\ln(1+R^2)$

NOTE.—$S \equiv 1 + 2R + 2(R+R^2)^{1/2}$.

form, as $R \to 0$, of $\Psi \to 1 - Ar^{2-\gamma}$. Here A is a constant that depends on α and γ. For all models with an r^{-3} power-law falloff at large radii, the asymptotic form as $R \to \infty$ is $\Psi \to A'\ln(R)/R$.

The distribution function for an equilibrium spherical system with an isotropic dispersion tensor depends only on the relative energy $\mathscr{E}$ and can be calculated from the density profile and potential through an Abel transform (BT):

$$F(\mathscr{E}) = \frac{1}{\sqrt{8}\pi^2}\left[\int_0^{\mathscr{E}} \frac{d^2\varrho}{d\Psi^2}\frac{d\Psi}{\sqrt{\mathscr{E}-\Psi}} + \frac{1}{\sqrt{\mathscr{E}}}\left(\frac{d\varrho}{d\Psi}\right)_{\Psi=0}\right]. \quad (3)$$

In all of the models that we will consider, the second term on the right-hand side is zero.

The integral that remains is evaluated numerically. The integrand diverges at one or both of the limits but this can be handled using standard techniques such as those found in Press et al. (1986). The DF is evaluated at values of $\mathscr{E}$ equally spaced in $\ln\mathscr{E}$ for $0 \le \mathscr{E} < \frac{1}{2}$ and equally spaced in $\ln(1-\mathscr{E})$ for $\frac{1}{2} \le \mathscr{E} \le 1$. Accuracy is checked by calculating the density profile from the DF:

$$\varrho(R) = 4\sqrt{2}\pi \int_0^\Psi F(\mathscr{E})(\Psi - \mathscr{E})^{1/2}d\mathscr{E} \quad (4)$$

and comparing with the exact expression. Typically, 2×10^4 integration points are required to guarantee 0.1% agreement over the range $R = 10^{-6}$ to 10^6.

In Figure 1 we compare DFs for the Hernquist and NFW profiles. The DFs in the regime $(1 - \mathscr{E}) \ll 1$ are nearly identical (up to a normalization constant). This is to be expected, since in this regime the systems are dominated by particles at small radii and the Hernquist and NFW profiles each have an r^{-1} cusp. While the DFs diverge in this limit, the mass at small radii is finite, as we will see in § 5.

The DFs for both the Hernquist and the NFW models decrease as $\mathscr{E} \to 0$. However, the decrease is slower in the NFW model, a reflection of the fact that the halo in this model is more extended. It is straightforward to determine
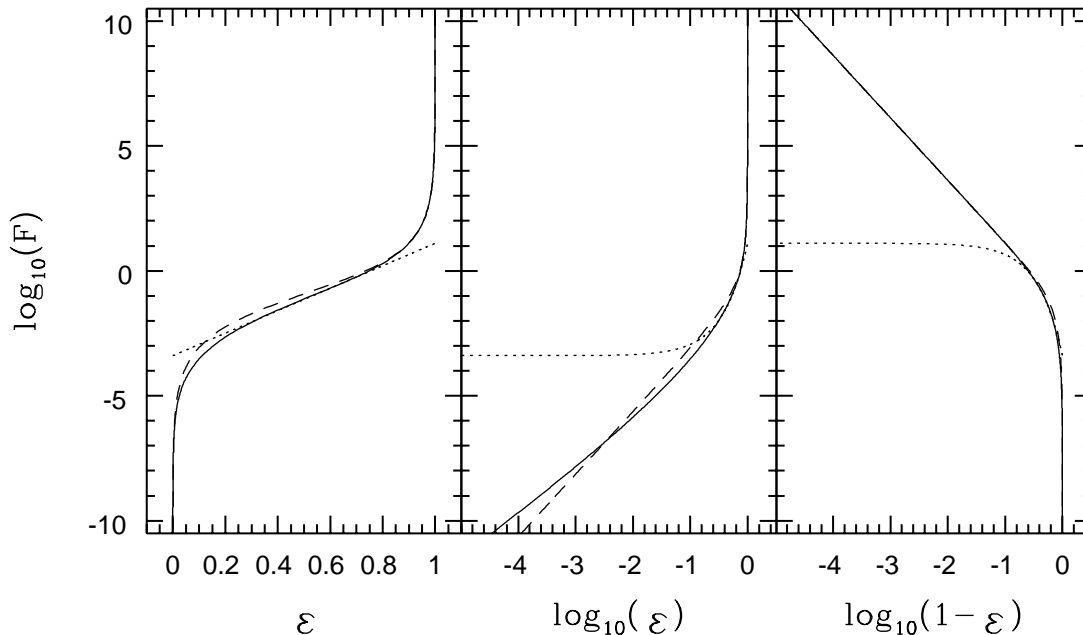

FIG. 1.—DFs as a function of relative energy $\mathscr{E}$ for the NFW profile (*solid curve*) and Hernquist profile (*dashed curve*)

the functional form of the DF in this limit. For the NFW model

$$\frac{d^2\varrho}{d\Psi^2} \simeq \frac{1}{R(\ln R)^2} \simeq \frac{\Psi}{(-\ln\Psi)^3} , \tag{5}$$

and we find

$$F(\mathscr{E}) \propto \frac{\mathscr{E}^{3/2}}{(-\ln\mathscr{E})^3} , \tag{6}$$

as compared with the Hernquist model, where $F \propto \mathscr{E}^{5/2}$.

The results for our series of $\alpha = 1$ models (I–IV) are plotted in Figure 2. All of the DFs in this series have a limiting form as $\mathscr{E} \to 0$ given, up to a constant, by equation (6). The difference in the index for the power-law cusp at small radii is reflected in the behavior of the DFs as $\mathscr{E} \to 1$, with the trend that a steeper inner cusp corresponds to a stronger divergence in this limit. Once again, we can determine a limiting form for the DF, this time as $\mathscr{E} \to 1$. For

$\gamma = (\frac{1}{2}, 1, \frac{3}{2})$, we have $d^2\rho/d\Psi^2 \propto R^{\gamma-4}$, and we find

$$F(\mathscr{E}) \propto \int_{R_\mathscr{E}}^{\infty} \frac{dR}{R^3[AR^{2-\gamma} - (1-\mathscr{E})]^{1/2}} \tag{7}$$

$$\propto (1-\mathscr{E})^{-(6-\gamma)/(4-2\gamma)} , \tag{8}$$

where $R_\mathscr{E}$ is defined by the relation $\Psi(R_\mathscr{E}) = \mathscr{E}$. In writing this expression, we use the fact that the integral is dominated by the region in $R \simeq R_\mathscr{E} \propto (1-\mathscr{E})^{1/(2-\gamma)}$. For the NFW profile, $F \propto (1-\mathscr{E})^{-5/2}$ which is the same as is found in the Hernquist model (Hernquist 1990). The case $\gamma = 0$ is handled separately: We find $d^2\rho/d\Psi^2 \propto R^{-3}$ and $F \propto (1-\mathscr{E})^{-1}$.

Kravtsov et al. (1998) suggest that the plausible value of the parameter α is $\alpha = 2$, corresponding to a sharper transition between inner and outer regions of the halo. In Figure 3 we compare the DFs for the two models $(\alpha, \beta, \gamma) = (1, 3, 0)$ and $(2, 3, 0)$. The most striking difference occurs as $\mathscr{E} \to 1$ (small radii), where the DF for the $\alpha = 2$ model approaches
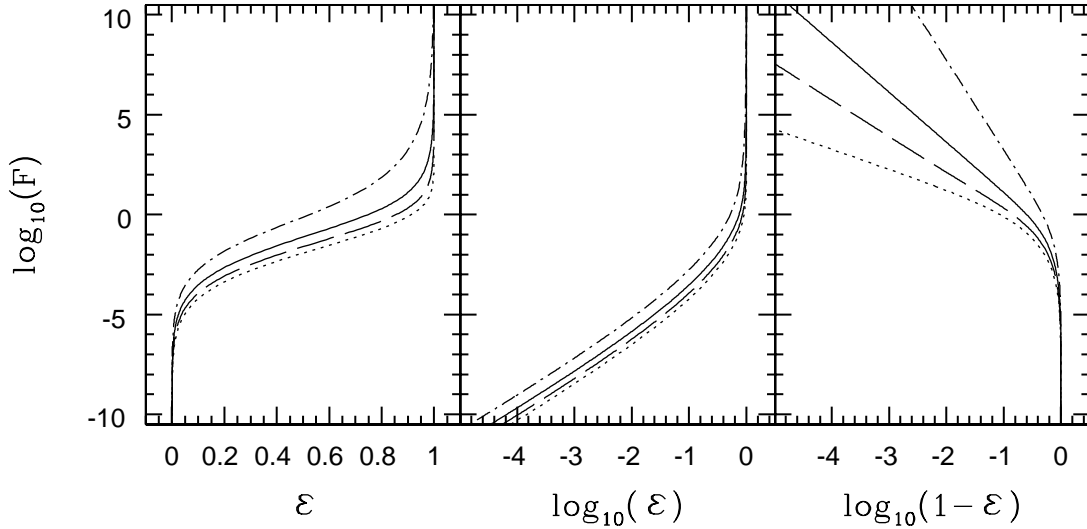

FIG. 2.—DFs for models I–IV ($\alpha = 1$; $\beta = 3$): model I, $\gamma = 0$ (*dotted curve*); model II, $\gamma = \frac{1}{2}$ (*long-dashed curve*); model III, $\gamma = 1$, the NFW profile (*solid curve*); model IV, $\gamma = \frac{3}{2}$ (*dot-dashed curve*).
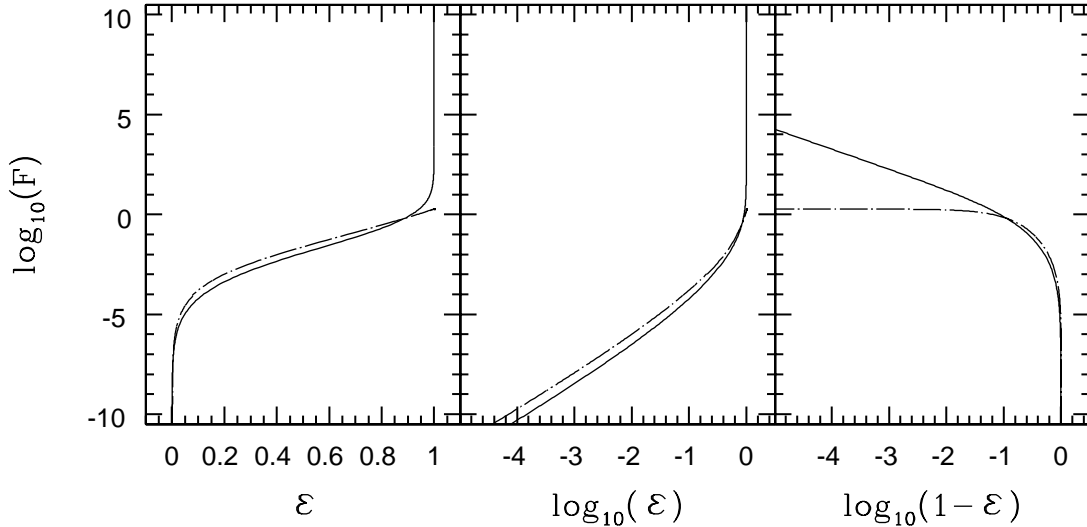

FIG. 3.—Comparison of the DFs for models I and V ($\gamma = 0$; $\beta = 3$): $\alpha = 1$ (*dotted curve*) and $\alpha = 2$ (*dot–long-dashed curve*)
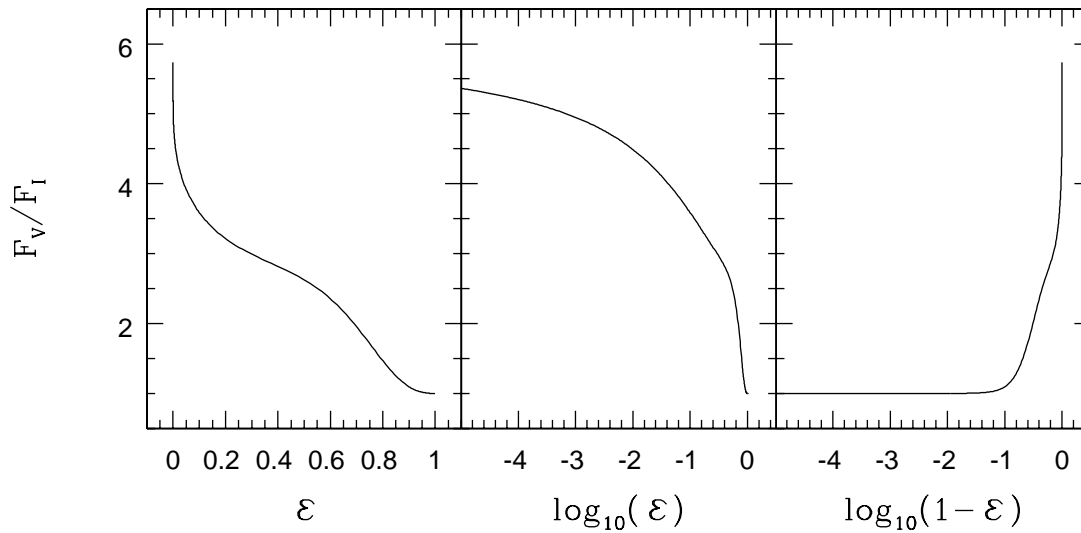
FIG. 4.—DF for model VI divided by the DF for model II

a constant. This can be understood by noting that as $R \to 0$, $d^2\varrho/d\Psi^2$ is finite for $\alpha = 2$; $\gamma = 0$ but diverges for $\alpha = 1$.

The distinction between the DFs for $(\alpha, \beta, \gamma) = (1, 3, 1)$ and $(2, 3, 1)$ is more subtle. The asymptotic forms as $\mathscr{E} \to 1$ and $\mathscr{E} \to 0$ are the same, and so the difference between the models arises solely in the transition region. In Figure 4 we plot the ratio of the DFs for the two models. If we normalize the models at $\mathscr{E} = 1$ ($R = 0$), then as $R \to \infty$ the DF for $\alpha = 2$ will exceed that for $\alpha = 1$ by a factor $\simeq 6$.

Physical DFs ($F \geq 0$ for $0 \leq \mathscr{E} \leq 1$) exist for all of the isotropic models considered here. Moreover, both F and $d^2\varrho/d\Psi^2$ are monotonically increasing functions of $\mathscr{E}$. This, by Antonov's second and third laws, is sufficient to guarantee that these models are stable against both radial and nonradial perturbations (BT).

3. DFS WITH ANISOTROPIC VELOCITY DISPERSION

The DF of any steady state system that is spherically symmetric in both velocity and configuration space can be expressed as a function $f(E, L)$ where L is the magnitude of the angular momentum vector (BT). In general, the velocity-dispersion tensors for these models are anisotropic: the velocity dispersions in the two tangential directions are equal but in general different from the velocity dispersion in the radial direction. We investigate a special class of these models in which the DF assumes the form (Osipkov 1979; Merritt 1985a, 1985b)

$$F(\mathscr{E}, \mathscr{L}) = F(Q) ,   (9)$$

where $\mathscr{L} = L/(4\pi G\rho_0 a^4)^{1/2}$ and $Q \equiv \mathscr{E} - \mathscr{L}^2/2R_a^2$. In addition, the condition $F = 0$ for $Q \leq 0$ is imposed. R_a is often called the anisotropy radius: outside R_a the velocity dispersion is peaked toward radial orbits, while inside R_a the dispersion is nearly isotropic. As discussed in Carollo et al. (1995), physical models do not exist for $R_a < R_{a,\min}$, where $R_{a,\min}$ depends on the shape of the potential and must be determined numerically. For values of R_a below this threshold, the DF must become negative for a range of values in Q
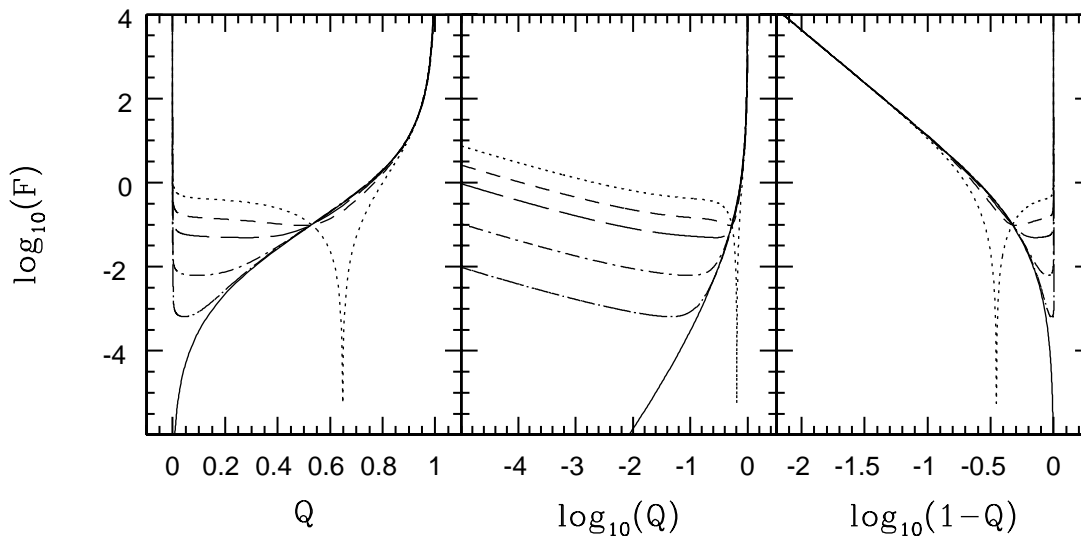

FIG. 5.—DF for the NFW profile assuming a velocity dispersion tensor of the type proposed by Osipkov and Merritt. The different curves correspond to different values of the anisotropy parameter R_a: $R_a = 0.35548$ (*dotted curve*); $R_a = 0.6$ (*dashed curve*); $R_a = 1$ (*long-dashed curve*); $R_a = 3$ (*dot-dashed curve*); $R_a = 10$ (*dot-long-dashed curve*). The DF assuming an isotropic dispersion tensor $R_a \to \infty$ (model III) is given by the solid curve.
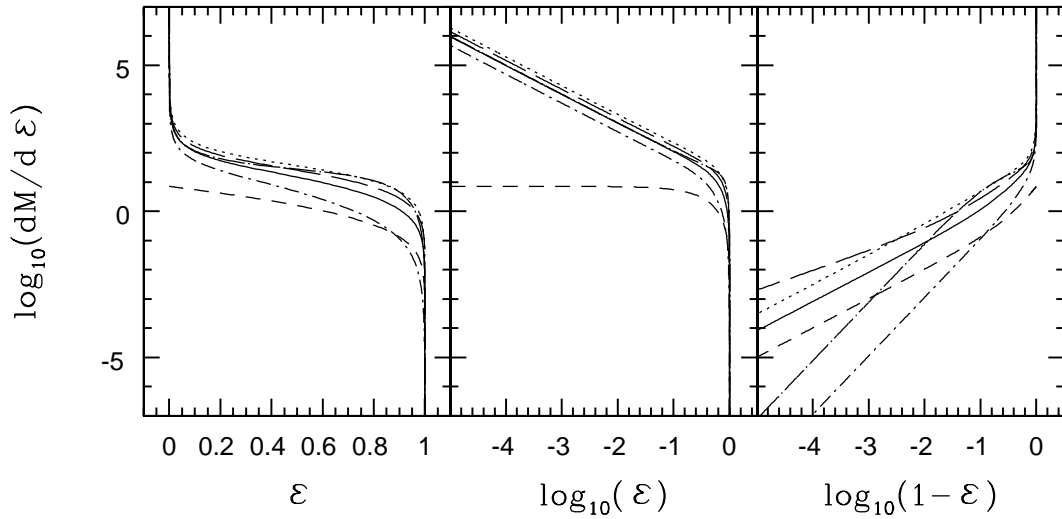
FIG. 6.—Differential energy distribution, $dM/d\mathscr{E}$, as a function of energy for models I–V and the Hernquist model. Curves are labeled as in Figs. 1 and 2.

in order to compensate for the excess population of radial orbits needed to produce the halo at large radii. The problem is more severe for the systems considered here, since the density profile at large radii varies as r^{-3} rather than r^{-4}. In particular, we find that $R_{a,\min} \simeq 0.36$ and 0.75 for $(\alpha, \beta, \gamma) = (1, 3, 0)$ and $(1, 3, 0)$ respectively. By comparison, Carollo et al. (1995) find $R_{a,\min} \simeq 0.20$ and 0.45 for $(\alpha, \beta, \gamma) = (1, 4, 0)$ and $(1, 4, 0)$, respectively (see their Fig. 1).

The DF for the Osipkov-Merritt models is found by replacing the ϱ in equation (3) with the auxiliary density $\varrho_Q \equiv (1 + R^2/R_a^2)\varrho$. The results for a sequence of Osipkov-Merritt NFW models is shown in Figure 5. The pathological nature of the DF as $R_a \rightarrow R_{a,\min}$ is evident in the dotted curve ($R_a = R_{a,\min} + \epsilon$, where $\epsilon \sim 10^{-5}$).

Notice that for these models the DF at small $\mathscr{E}$ is a decreasing function of $\mathscr{E}$ ($F \propto \mathscr{E}^{-1/2}$). Stability analysis against radial perturbations by application of Antonov's second law is therefore inconclusive (BT). While models with $R_a \rightarrow \infty$ are stable against both radial and nonradial perturbations, those with $R_a \rightarrow 0$ are almost certainly

unstable to radial perturbations (Merritt 1985b). Numerical experiments are therefore required to determine the exact region of stability.

4. DIFFERENTIAL ENERGY DISTRIBUTION

When comparing results of N-body simulations with those from analytic models, it is natural to use the differential energy distribution $dM/d\mathscr{E}$ (BT). For models with an isotropic velocity dispersion tensor, $dM/d\mathscr{E}$ is simply the product of the DF with the density of states:

$$\frac{dM}{d\mathscr{E}} = F(\mathscr{E})G(\mathscr{E}) , \qquad (10)$$

where

$$G(\mathscr{E}) = 16\sqrt{2}\pi^2 \int_0^{R_{\mathscr{E}}} (\Psi - \mathscr{E})^{1/2} R^2 \, dR ; \qquad (11)$$

M is a dimensionless mass variable scaled by $\rho_0 a^3$. Note that as $\mathscr{E} \rightarrow 0$, $G(\mathscr{E}) \propto \mathscr{E}^{-5/2}$ (up to logarithmic corrections)
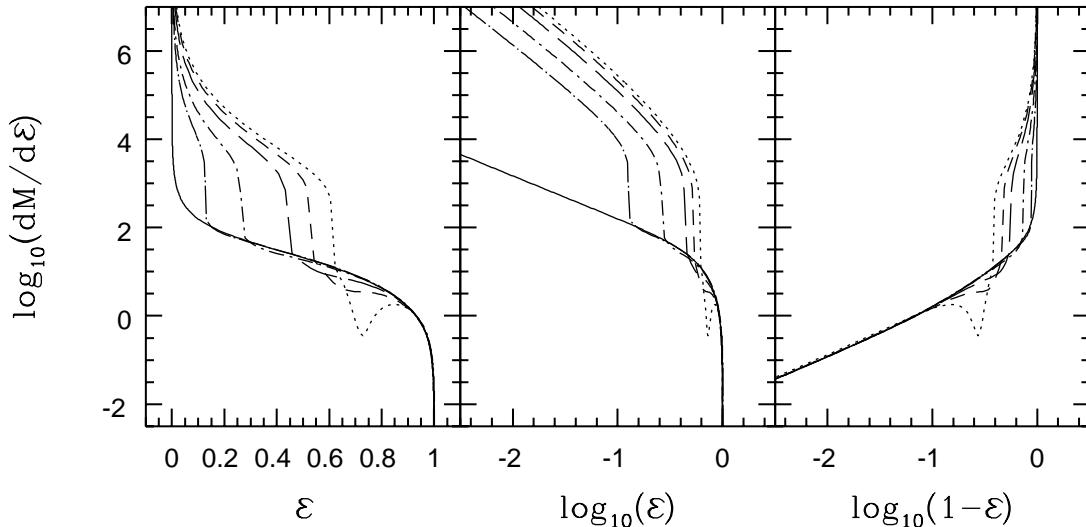

FIG. 7.—$dM/d\mathscr{E}$ for the anisotropic models. Curves are labeled as in Fig. 5.

for both the models considered here and the Hernquist model.

Figure 6 is a plot of $dM/d\mathscr{E}$ for models I–V and for the Hernquist model. In the limit $\mathscr{E} \to 0$, $dM/d\mathscr{E}$ for the Hernquist model approaches a constant, reflecting the fact that the total mass is finite. Conversely, for the models considered here, $dM/d\mathscr{E}$ diverges as $\mathscr{E}^{-1}$, a symptom of the logarithmic mass divergence at large radii.

It is a somewhat more difficult exercise to calculate the differential energy distribution for Osipkov-Merritt models. Let us begin, as is done in the derivation of equation (10), with the expression for the total mass within a radius R (BT):

$$M(R) = 16\pi^2 \int_0^R R'^2 \, dR' \int_0^{\Psi(R')} v \, d\mathscr{E}$$
$$\times \int_0^{\pi/2} F(\mathscr{E}, RV \sin \eta) \sin \eta \, d\eta , \qquad (12)$$

where η is the polar angle in velocity space: $V_r \equiv V \cos \eta$. We first replace the integration variable η with Q using the relation $Q \equiv \mathscr{E} - \frac{1}{2}(R/R_a)^2 V^2 \sin^2 \eta$ and then interchange the R and $\mathscr{E}$ integrations to find

$$M(R) = 8\sqrt{2}\pi^2 R_a \int_0^1 d\mathscr{E} \int_0^{R_\mathscr{E}} R' \, dR' \int_{\mathscr{E}-\bar{\mathscr{E}}}^{\mathscr{E}} \frac{F(Q)dQ}{[Q - (\mathscr{E} - \bar{\mathscr{E}})]^{1/2}} ,$$
$$(13)$$

where $\bar{\mathscr{E}} \equiv \frac{1}{2}(R'/R_a)^2 V^2$. Thus, the differential energy distribution for the Osipkov-Merritt models can be evaluated by performing the double integral

$$\frac{dM}{d\mathscr{E}} = 8\sqrt{2}\pi^2 R_a \int_0^{R_{\min}} R' \, dR' \int_{\mathscr{E}-\bar{\mathscr{E}}}^{\mathscr{E}} \frac{F(Q)dQ}{[Q - (\mathscr{E} - \bar{\mathscr{E}})]^{1/2}} , \quad (14)$$

where $R_{\min} = \min(R_\mathscr{E}, R)$. It is straightforward to show that in the limit $R_a \to \infty$, $\bar{\mathscr{E}} \to 0$ and equation (14) reduces to equation (10).

The results for the four NFW models considered in § 3 are shown in Figure 7. Note that the divergence as $\mathscr{E} \to 0$ is even more severe $(dM/d\mathscr{E} \propto \mathscr{E}^{-2})$.

5. APPLICATIONS

In this section three possible applications of the results presented above are briefly discussed.

5.1. *Initial Conditions for N-Body Experiments*

The dynamic range in N-body simulations has now reached the level where it is possible to study individual halos in exquisite detail while maintaining an accurate representation of the large-scale tidal fields that shape them. Nevertheless, it is often useful to conduct highly controlled, albeit artificial, numerical experiments in order to gain a better understanding of the processes at work during halo formation. For example, numerous groups have used numerical simulations to study the accretion of satellites with a parent halo as well as the merger of two halos of comparable mass. Another set of experiments follows the evolution of a gas and dark matter system in order to better understand the process of disk formation. Typically, very simple DFs (e.g., truncated isothermal sphere, Plummer model) are used to set up the initial conditions for these experiments, and the choice is often made out of convenience, i.e., the availability of analytic DFs, rather than an expectation of what might arise in a cosmological setting.

The DFs found in this work allow one to set up a variety of halo models with various forms for the density profile and velocity distribution tensor. For the models with isotropic velocity dispersion tensors, the probability for a particle to have energy $\mathscr{E}$ and radius R is

$$P(\mathscr{E}, R) \propto R^2 (\Psi - \mathscr{E})^{1/2} F(\mathscr{E}) . \qquad (15)$$

The rejection method described, for example, in Press et al. (1986) provides a simple technique for selecting particles from this distribution. Once $\mathscr{E}$ and R for a given particle are known, the speed V can be determined immediately. One then chooses, at random, four angles (two in configuration space and two in velocity space) to yield the six phase-space coordinates of the particle. This procedure can be extended easily to the Osipkov-Merritt models.

5.2. *Interpretation of Results from Dark Matter Search Experiments*

The announcements in 1993 by the MACHO (Alcock et al. 1993) and EROS (Aubourg et al. 1993) collaborations of candidate microlensing events toward the LMC have highlighted the need for self-consistent model DFs of the Galaxy's halo. Interpreting the results from these experiments requires a comparison of the observed and predicted event rates. The latter has now been calculated for a set of halo models too numerous to list here. These models are generally constructed in one of two ways. One can begin with an *Ansatz* for the mass distribution (e.g., triaxial spheroid with a prescribed density law) and assume a simple form for the velocity dispersion tensor (e.g., isotropic and Maxwellian). Of course, models constructed in this manner do not, in general, correspond to true equilibrium systems, i.e., solutions of the time-independent collisionless Boltzmann equation. A second approach employs exact, analytic model DFs. Here the Jeans theorem is invaluable, since it allows one to construct model DFs simply by taking functions of the integrals of motion. The so-called power-law models in which the DF is constructed from powers of the energy and the angular momentum vector L_z (Evans 1994) have been used in this way (Evans & Jijina 1994).

The DFs presented in this work provide an alternative set of models suitable for the analysis and interpretation of results from dark matter search experiments. The density profiles include many of the popular forms found in the literature. In addition, the Osipkov-Merritt *Ansatz* for velocity-space anisotropy is consistent with what one expects for a realistic halo model, i.e., primarily radial orbits in the outermost regions of the halo where particles have only recently separated from the Hubble flow.

5.3. *Formation of Dark Matter Halos*

The hierarchical clustering hypothesis provides a compelling picture for the formation of structure in a universe dominated by cold, dissipationless dark matter. This scenario naturally lends itself to the development of phenomenological models for the growth of dark matter halos (e.g., the Press-Schechter formalism [Press & Schechter 1974]). Nevertheless, hierarchical clustering says little about the internal structure of these systems. For this, one must understand the process by which a collisionless system relaxes to an equilibrium or quasi-equilibrium state. To this end, two opposing pictures have emerged. The first suggests that violent relaxation is the dominant process at work, the conjecture being that particles will transfer energy to one

another as they move through the rapidly varying potential of the collapsing system. In so doing, the particles lose all memory of their initial state. The alternative picture is based on the spherical infall model (Gunn & Gott 1972; Fillmore & Goldreich 1984; Bertschinger 1985), in which a system relaxes from the inside out. Particles near the peak of the initial density perturbation collapse first and constitute the most tightly bound regions of the final system. Likewise, particles in the wings of the initial density perturbation collapse later on and form the system's outer halo. Here one expects a direct correspondence between initial conditions and the final state of the system and, in particular, a tight correlation between initial and final energy and angular momentum.

Not surprisingly, the dark matter halos found in cosmological simulations appear to follow an intermediate path in reaching a relaxed or virialized state. Quinn & Zurek (1988) track the binding energy and angular momentum of selected particles during the simulated formation of a dark matter halo. They conclude that although energy and angular momentum are not conserved, the collapse is more orderly than one would predict assuming violent relaxation. Indeed, there seems to be a tight correlation between initial and final energy and angular momentum. The suggestion, then, is that there is a simple relation between the differential energy and angular momentum distributions of a relaxed system and the initial perturbation that gave rise to it. The DFs presented in this work may provide a further link between the $dM/d\mathscr{E}$ or $d^2M/d\mathscr{E}d\mathscr{L}$ and the density profile.

6. CONCLUSION

The density profile and associated gravitational potential provide a popular way of characterizing dark matter halos. To be sure, the halos found in simulations are varied in shape and rich in substructure. However, it is essentially the density profile that determines the contribution by the halo to the observed rotation curve. Moreover, the evolution of the gas component (e.g., in forming a disk galaxy) depends sensitively on the shape and depth of the potential.

In this paper, we have presented DFs that reproduce six different density profiles. All of the models assume spherical symmetry and a power-law falloff at large radii $\rho \propto r^{-3}$ but differ in the slope of the inner power-law cusp and the sharpness of the transition in going from inner to outer regions of the halo.

We have considered models with velocity-space anisotropy of the type proposed by Osipkov and Merritt. The key feature and also limitation of these models is that the distribution of orbits varies from one that is nearly isotropic in the inner regions of the halo to one that is nearly radial in the outer regions. In addition, since the Osipkov-Merritt models provide a family of DFs, parameterized by R_a, that reproduce the same density profile, they may be combined to yield a fairly general class of models (Merritt 1985a).

Although the DFs presented in this work were derived numerically, the analytic fitting formulae provided in the Appendix should enable researchers to use them with the same ease they would experience with closed-form DFs such as the Hernquist model.

Note added in manuscript.—Following the completion of this paper, I learned that some of the results related to the NFW model (isotropic velocities) have also been derived by Lokas & Mamon (2000).

APPENDIX

In this appendix, we provide analytic fitting formulae for some of the DFs presented in the text. The limiting forms for the isotropic models, as discussed in the text, are

$$F(\mathscr{E}) \propto \begin{cases} \mathscr{E}^{3/2}(-\ln \mathscr{E})^{-3} & \text{for } \mathscr{E} \to 0 \,, \\ (1 - \mathscr{E})^{-\lambda} & \text{for } \mathscr{E} \to 1 \,, \end{cases} \tag{A1}$$

where $\lambda = (1, 11/6, 5/2, 9/2, 0, 5/2)$ for models I–VI, respectively. Noting that $-\ln \mathscr{E} \simeq (1 - \mathscr{E})$ for $1 - \mathscr{E} \ll 1$, we propose the following fitting formulae for the isotropic DFs:

$$F(\mathscr{E}) = F_0 \, \mathscr{E}^{3/2} (1 - \mathscr{E})^{-\lambda} \left(\frac{-\ln \mathscr{E}}{1 - \mathscr{E}} \right)^q e^P \,, \tag{A2}$$

TABLE 2

FITTING FORMULA PARAMETERS FOR ISOTROPIC MODELS

Model	F_0	q	p_1	p_2	p_3	p_4	p_5	p_6
I........	2.0460×10^{-2}	-2.7145	-1.0215	23.766	-98.330	194.50	-180.01	63.296
II.......	3.6478×10^{-2}	-2.7092	0.8670	-10.035	65.895	-166.31	179.21	-70.007
III......	9.1968×10^{-2}	-2.7419	0.3620	-0.5639	-0.0859	-0.4912	$\ldots$	$\ldots$
IV	4.8598×10^{-1}	-2.8216	0.3526	-5.1990	3.5461	-0.8840	$\ldots$	$\ldots$
V	5.8807×10^{-2}	-2.6312	-3.7147	41.045	-132.20	216.90	-170.23	51.606
VI	1.4696×10^{-1}	-2.6210	-3.6125	23.172	-78.104	135.80	-123.11	43.705

TABLE 3

FITTING FORMULA PARAMETERS FOR ANISOTROPIC MODELS

R_a	F_0	q	p_1	p_2	p_3	p_4	p_5	p_6
0.6	1.0885×10^{-1}	-1.0468	-1.6805	18.360	-151.72	336.71	-288.09	85.472
1	3.8287×10^{-2}	-1.0389	0.3497	-12.253	-9.1225	101.15	-127.43	47.401
3	4.2486×10^{-3}	-1.0385	0.7577	-25.283	149.27	-282.53	229.13	-69.048
10	3.8951×10^{-4}	-1.0447	-2.2679	79.474	-237.74	329.07	-223.43	59.581

where the polynomial $P \equiv \sum_i p_i \mathscr{E}^i$ is introduced to improve the fit. In general, 3–5 terms in P are required to achieve a reasonable fit. The parameters are given in Table 2. Notice that $q \simeq -3$ as is expected from equation (A1).

For the anisotropic models discussed in the text ($\alpha = 1$; $\gamma = 1$), we use the fitting formula

$$F(Q) = F_0 \, Q^{-1/2} (1 - Q)^{-\lambda} \left(\frac{-\ln Q}{1 - Q} \right)^q e^P \, , \qquad (A3)$$

where P is now a polynomial in Q. The parameters are given in Table 3. No attempt is made to fit the DF for $R_a \simeq R_{a,\min}$.

REFERENCES

Alcock, C., et al. 1993, Nature, 365, 621
Aubourg, E., et al. 1993, Nature, 365, 623
Bertschinger, E. 1985, ApJS, 58, 39
Binney, J., & Tremaine, S. 1987, Galactic Dynamics (Princeton: Princeton Univ. Press), chaps. 4 and 5 (BT)
Carollo, C. M., de Zeeuw, P. T., & van der Marel, R. P. 1995, MNRAS, 276, 1131
Evans, N. W. 1994, MNRAS, 267, 333
Evans, N. W., & Jijina, J. 1994, MNRAS, 267, L21
Fillmore, J. A., & Goldreich, P. 1984, ApJ, 281, 1
Gunn, J., & Gott, J. R. 1972, ApJ, 176, 1
Henriksen, R. N., & Widrow, L. M. 1999, MNRAS, 302, 321
Hernquist, L. 1990, ApJ, 356, 359
Kravtsov, A. V., Klypin, A. A., Bullock, J. S., & Primack, J. R. 1998, ApJ, 502, 48
Lokas, E. L., & Mamon, G. A. 2000, MNRAS, in press (astro-ph/0002395)
Lynden-Bell, D. 1967, MNRAS, 136, 101
Merritt, D. 1985a, AJ, 90, 1027
———. 1985b, MNRAS, 214, 25P
Merritt, D., Tremaine, S., & Johnstone, D. 1989, MNRAS, 236, 829
Moore, B., Governato, F., Quinn, T., Stadel, J., & Lake, G. 1998, ApJ, 499, L5
Navarro, J. F., Frenk, C. S., & White, S. D. M. 1996, ApJ, 462, 563
Osipkov, L. P. 1979, AZh Pis'ma, 5, 77
Press, W. H., Flannery, B. P., Teukolsky, S. A., & Vetterling, W. T. 1986, Numerical Recipes (Cambridge: Cambridge Univ. Press), chaps. 3, 4, and 9
Press, W. H., & Schechter, P. 1974, ApJ, 187, 425
Quinn, P. J., & Zurek, W. H. 1988, ApJ, 331, 1
Tremaine S. 1987, in Structure and Dynamics of Elliptical Galaxies, ed. T. de Zeeuw (Dordrecht: Reidel), 367